Proceedings of the ASME 2023
Pressure Vessels & Piping Conference
PVP2023
July 16-21, 2023, Atlanta, Georgia, USA

PVP2023-107347

POST IRRADIATION EXAMINATION OF PRESSURIZED WATER REACTOR STAINLESS STEEL INTERNAL COMPONENTS

Timothy G. Lach and Xiang Chen

Materials Science and Technology Division, Oak Ridge National Laboratory, Oak Ridge, TN, USA

ABSTRACT

Internal structural components of pressurized water reactors (PWR), such as baffle former bolts, are subjected to significant neutron irradiation and mechanical stresses at elevated temperatures during plant operation. Over the long operation of the power plant, these conditions lead to potential degradation and reduced load-carrying capacity of these bolts. To understand property degradation more fully, to confirm the results of experimental irradiation programs, and to predict operational lifetime performance of structural materials in internal components, post irradiation examination of harvested materials from operating nuclear reactors is required. In this work, two high fluence 316 stainless steel baffle former bolts were retrieved from a commercial Westinghouse two-loop downflow type PWR and then sectioned for analysis via mechanical testing and microstructural characterization. The irradiation damage fluctuated along the bolt length with damage levels from 15 to 41 displacements per atom with the bolt head receiving approximately twice the neutron damage levels as that of the bolt thread section. Mechanical testing evaluations showed extensive irradiation hardening and a sharp decrease in fracture toughness in all parts of the bolt, though with limited variation along the bolt length. Microstructural characterization using analytical scanning transmission electron microscopy and atom probe tomography showed significant radiation induced precipitation, segregation, and dislocation loop and cavity formation. However, unlike the mechanical behavior, there was considerable variation along the bolt length but opposite of what may be expected, with more precipitation and cavity formation in the bolt thread where the radiation dose is less than in the bolt head where radiation dose is higher. The cause of this variation is likely due to gradients in temperature, neutron energy, and gamma irradiation.

Keywords: Post irradiation examination, radiation effects, austenitic stainless steel, nuclear reactor internals

1. INTRODUCTION

Internal components of nuclear reactors are subjected to multiple environmental extremes such as high radiation doses, high temperatures, corrosive environments, and mechanical stresses. The degradation and reduction in load-carrying ability of internal components may make it difficult to extend the lifetime of existing pressurized water reactors (PWR). Thus, it is important to understand how the microstructures and properties evolve during irradiation for evaluation of lifetime extension of existing light water reactors. As one of the PWR internal components, baffle-former bolts (BFBs) are subjected to significant mechanical stress and neutron irradiation from the reactor core during the plant operation. Susceptibility to a loss of ductility, swelling, and stress-corrosion cracking (SCC) are three of the primary concerns in austenitic stainless steel reactor internal components [1]. These are present due to radiation-induced precipitation and dislocation loop formation, radiation-induced segregation (RIS), and void formation and growth [2]. Dislocation loop formation and Ni-Si precipitation contribute to hardening; void formation contributes to swelling; and Ni and Si RIS to grain boundaries likely contributes to SCC. The stress, neutron flux, and temperature in BFBs varies significantly along the length of the bolt, which means it can be used to study radiation effects as a function of neutron flux, temperature, and/or stress gradients, which may enhance susceptibility of component failure. Indeed, the BFB has been a particular concern for the nuclear industry since the 1980s when the failed bolts were first observed [3]. In support of evaluating long-term operational performance of materials used in core internal components, the Materials Research Pathway (MRP) under the

U.S. Department of Energy (DOE) Light Water Reactor Sustainability (LWRS) Program pursued the retrieval of aged structural components for the study of the microstructure, mechanical, and corrosion-related properties including SCC and irradiation-assisted SCC (IASCC) initiation and growth. To this end, the MRP successfully harvested two high fluence BFBs with variation in neutron radiation dose from a Westinghouse two-loop downflow type PWR in 2016. The specimens were shipped to Oak Ridge National Laboratory (ORNL) for further testing and post irradiation examination [4–6].

The objective of this project is to provide information that is integral to evaluating end of life microstructure and properties as a benchmark of international models developed for predicting radiation-induced swelling, segregation, precipitation, and mechanical property degradation. In this study, post irradiation examination via microstructural characterization and mechanical testing were conducted to analyze the microstructure and properties evolution at different sections of each bolt. The 316 stainless steel bolts were subjected neutron radiation fluxes ranging from 15 displacements per atom (dpa) in the thread section of the lower dose bolt up to 41 dpa in the bolt head of the higher dose bolt, enabling study of dose effects on microstructure and property evolution. The mechanisms for microstructure evolution were interrogated using high magnification and high-resolution advanced techniques including transmission electron microscopy (TEM), analytical scanning TEM (STEM), and atom probe tomography (APT). Together, these techniques will tie together how the microstructure changes compare with the mechanical behavior evolution with respect to hardness and fracture toughness. The focus of this article will primarily be on the microstructural evolution and tying this to changes in mechanical behavior. Results from this study specifically fill the knowledge gaps for the mechanisms of radiation-induced precipitation and cavity formation as a function of radiation temperature and radiation dose for type 316 austenitic stainless steels used in commercial PWR power plants.

2. MATERIALS AND METHODS

2.1 Materials

Two 316 stainless steel baffle former bolts (BFB) were harvested from a Westinghouse two-loop downflow type pressurized water reactor (PWR), with the highest fluence among bolts withdrawn from service in 2011. Both bolts showed no indication of cracking during the ultrasonic inspection and in visual inspection following removal from service. However, the bolts required a lower torque for removal from the baffle structure than the original torque specified during installation, which may signify degradation in load carrying capability. Fig. 1 shows images of the bolt heads of two retrieved BFBs. No indication of surface cracking was observed in the transition region between the shaft and head, although some surface debris scale flaked off from the bolt body. The composition in both atomic percent (at%) and weight percent (wt%) for the two bolts, designated as 4412 and 4416, as determined by atom probe tomography (APT) is presented in Table 1. The bolts are within specifications for type 316 stainless steel with slightly elevated Cr content, but this could be due to local variations.

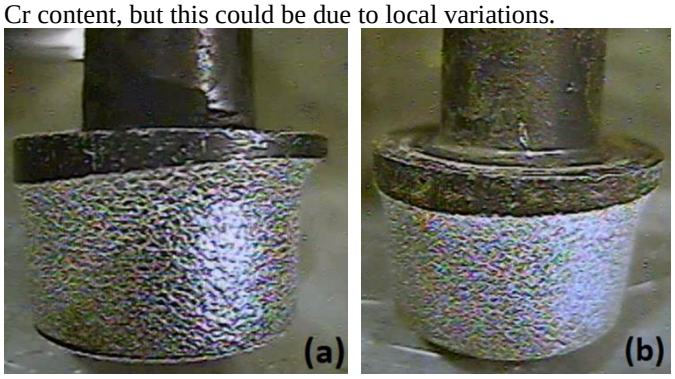

FIGURE 1: Images of bolt heads for (a) bolt 4412 and (b) bolt 4416; speckled look on bolt heads are from machining after removal from service.

TABLE 1: Composition of bolts 4412 and 4416 from APT reconstructions

	BFB-4412		BFB-4416		316-SS Spec
Element	At%	Wt%	At%	Wt%	Wt%
Fe	64.19	64.62	64.56	64.96	Bal.
Ni	11.55	12.22	11.39	12.04	10.00-14.00
Cr	19.32	18.11	19.36	18.14	16.00-18.00
Mn	1.62	1.60	1.67	1.65	2.00 max
Mo	1.18	2.04	1.18	2.04	2.00-3.00
Si	1.24	0.63	1.15	0.58	1.00 max
C	0.20	0.043	0.19	0.040	0.08 max
P	0.024	0.013	0.027	0.15	0.040 max
Cu	0.26	0.29	0.25	0.28	0.75 max

Table 2 provides information on the range of fluences and estimated displacement damage along the length of the two bolts. The displacement damage values for the two bolts range from 15 to 41 dpa assuming a fluence to dpa conversion value of 6.7×10^{20} n/cm^2, E > 1 MeV per dpa [2]. Other important information for the two retrieved bolts not available at the time of preparation of this report includes the irradiation temperature profile, irradiation flux, and thermomechanical stress state. These require more complicated modeling and calculation and can vary within each power cycle and from cycle to cycle. For instance, calculations [7] from Point Beach Unit 2, which is another Westinghouse two-loop type PWR, showed that the irradiation temperature and flux for a BFB from a region next to the bolts studied in this work varied in the range of 323-344 °C and 7.5×10^{12}-1.8×10^{13} n/cm^2-sec (E > 1 MeV) along the length of the bolt, respectively. Similarly, a baffle-former bolt removed from the Tihange 1 PWR showed a variation in irradiation temperature of about 23 °C (320-343 °C) along the bolt and a damage dose that was 2.6× higher in the bolt head (19.5 dpa) than the bolt thread (7.5 dpa) [8]. Further thermal variation along the bolt length in PWR baffle-former bolts was modeled with a high temperature of 340 °C in the mid-shank region and a low temperature of 288 °C in the bolt head region [9]. Therefore, the value for a detailed calculation on irradiation temperature and

flux of BFBs may be limited due to the large variation of those parameters during the lifetime of a BFB. It is worth noting that Point Beach Unit 2 was originally a Westinghouse two-loop downflow type PWR but was converted to upflow in November 1986, which could affect irradiation temperature and neutron flux [7].

TABLE 2: Fluence and estimated displacement damage distributions for the two retrieved baffle-former bolts

Bolt #	Fluence (10^{22} n/cm^2, E > 1MeV)/Estimated dpa		
	Head (CS)	Mid-shank (MS)	Mid-thread (BS)
4412	2.78/41	2.27/34	1.46/22
4416	1.91/29	1.56/23	1.00/15

For each BFB, four bend bar specimens and seven thin slice specimens were machined. The bend bar specimens were used in the fracture toughness and fatigue crack growth rate studies, whereas the thin slice specimens are planned for subscale tensile and microstructural analyses. Specimens were machined from different fluence regions of each bolt, allowing for studies of the effect of fluence on the microstructural and mechanical properties of BFBs.

2.2 Characterization Methods

Detailed TEM and APT characterizations were performed on the thin slice specimens and needle-shaped specimens prepared by focused-ion-beam/ scanning electron microscopy (FIB/SEM). In detail, after mechanically polished to mirror-surface conditions, thin slice specimens from BS, MS, and CS sections were loaded into an FEI Versa3D FIB/SEM DualBeam™ system, where lamella-type samples were lifted-out from the specimens for TEM characterizations and needle shaped-type specimens were lifted-out and shaped for APT characterizations. The TEM sample preparation followed the procedures of initial trenching, cutting, and thinning to 200 nm with 30 keV Ga ion beam, rough polishing to 100 nm with ion beam energy gradually reduced from 16 keV to 8 and 5 keV, and fine polishing with 2 keV ion beam to remove most FIB-induced damage. Before loading into the TEM, samples were always cleaned with a Fischione 1020 Plasma Cleaner for 10 minutes on each side using 900 eV Ar ions.

Conventional TEM characterization of radiation-induced damage and cavities were conducted using a JEOL 2100F field-emission-gun TEM operated at 200 keV. Cavities were identified by comparing underfocused and overfocused images from the same area, providing for quantification of cavity size and distributions. STEM/Energy-dispersive X-ray spectroscopy (EDS)-based mapping was performed using a Thermo (formerly FEI) Talos F200X STEM equipped with the SuperX 4-sector X-ray EDS system. Precipitates and dislocations were imaged using on [001]-zone axis bright field (BF), annular dark field (ADF), and high angle ADF (HAADF) imaging conditions [10]. Beam conditions were ~1-2 nA and 200 keV. X-ray spectrum images were acquired with a rate of ~20,000 counts/second for a duration of about one hour, and then maps of the relevant X-rays lines were extracted via post-processing [11].

APT was performed on a Cameca LEAP 4000XHR using laser pulse mode with a laser energy of 60 pJ, detection rate of 0.005 atoms/pulse, pulse repetition rate of 200 kHz while maintaining needle specimen temperature at ~40 K. Reconstructions and analyses for APT were performed using Cameca's Integrated Visualization and Analysis Software 3.8.10 (IVAS) using techniques that include radial distribution functions analysis, frequency distribution analysis, and isoconcentration surface (isosurface)-based cluster analysis [12–14]. Similar mass/charge range files with only minor adjustments in the widths of selected peaks between reconstructions were used to reduce potential artefacts in compositional analyses among the various samples. The tip profile reconstruction method was used for determining the initial radius of the reconstruction using high resolution SEM images of the final tip. A fixed image compression factor of 1.65 and k-factor of 3.30 was used as no clear pole locations were found within the field ion micrographs. Global background subtraction was used for determining composition. Peak overlaps were considered and adjusted based on relative natural abundance of specific isotopes and preferred evaporation charge state; in general, these overlaps had a minimal effect for the purposes of this study as the greatest overlap accounted for less than 5% of a particular element (isotope 54 with overlaps for Cr and Fe).

Cluster analysis in APT data is a common unsupervised machine learning problem, and like many other problems in this category, it lacks a clear metric/loss function to define a quality of prediction or a confidence level of the result. In this study, the isosurface method for Ni, Si, Mo, and Cu clusters identification [15,16]. It is a simple and widely used technique to identify clusters by constructing a constant concentration surface based on local solute concentration, and the enclosed ions are identified as a cluster. This technique has great flexibilities and needs only one user input as concentration threshold. The concentration threshold is kept constant for all datasets since we are interested in the cluster size evolution, which is directly affected by the threshold choice. However, the selection of parameters may lead to some uncertainties for cluster identification in conditions where precipitation is low (i.e., low temperature thermal aging or irradiation). This is due to some clusters having much lower solute concentration in these conditions. However, we believe the corresponding volume fraction trend is preserved despite the minor uncertainties.

3. RESULTS AND DISCUSSION

TEM and analytical STEM characterization revealed a large degree of grain boundary segregation and precipitate, cavity, and dislocation loop formation. Using TEM/STEM observation, the heavily evolved microstructures were present in much the same degree in all three sections (BS, MS, and CS) of both BFBs. Much of the TEM examination of the lower dose BFB 4416 is found in the DOE report in Ref. [4]. An example of the precipitation and RIS is shown in the STEM BF and HAADF imaging and STEM-EDS element maps in Fig. 2 of a high angle

grain boundary in the MS section of BFB 4412. In the matrix, looking at the STEM-BF image, there are a high density of small dislocation loops. In the STEM-EDS maps, there is a high density of Ni-Si-rich precipitates within the grain interiors. There are also occasional Cr-rich clusters and P-rich clusters. Interestingly, the few Cr-rich precipitates appear to be adjoined to the Ni-Si precipitates. At the gain boundary, there three observations: RIS of Ni, Si, and P, a Ni-Si precipitate denuded zone within about 20-30 nm of the grain boundary, and large precipitates of a Ni-Si-Mn-rich phase. The width of the Ni, Si, and P rich segregation is very thin (< 6 nm). Outside this RIS is a zone where there are no precipitates found, a result of the mass balance between segregation of Ni and Si to the grain boundary from the matrix, leaving the local matrix too depleted in Ni and Si to precipitate a new phase. Not shown here but consistent with other published work, no segregation was observed at low angle grain boundaries or twin boundaries [17]. This difference between LAGB and HAGB segregation was observed in both BFBs. One observation at the grain boundary was different among the different sections of the bolts: the precipitation of the Ni-Si-Mn-rich phase. These occasional relatively large precipitates with a composition similar to G-phase ($Ni_{16}Si_7Mn_6$) were only found in the MS and BS sections of the BFBs. This phase is often found mostly in the ferrite phase after aging or irradiation in cast austenitic or duplex stainless steels at temperatures above 300 °C [18,19]. The lack of these precipitates in the CS or bolt head section hints that the temperature in this region was indeed below 300 °C, and the presence in the BS and MS sections highlights that these sections are exposed to a higher temperature, likely due to excess gamma heating. In the absence Ni and Si in the nearby matrix within the precipitate denuded zone, the driving force for Mn to cluster together at the grain boundary with the excess Ni and Si may be high enough due to RIS.

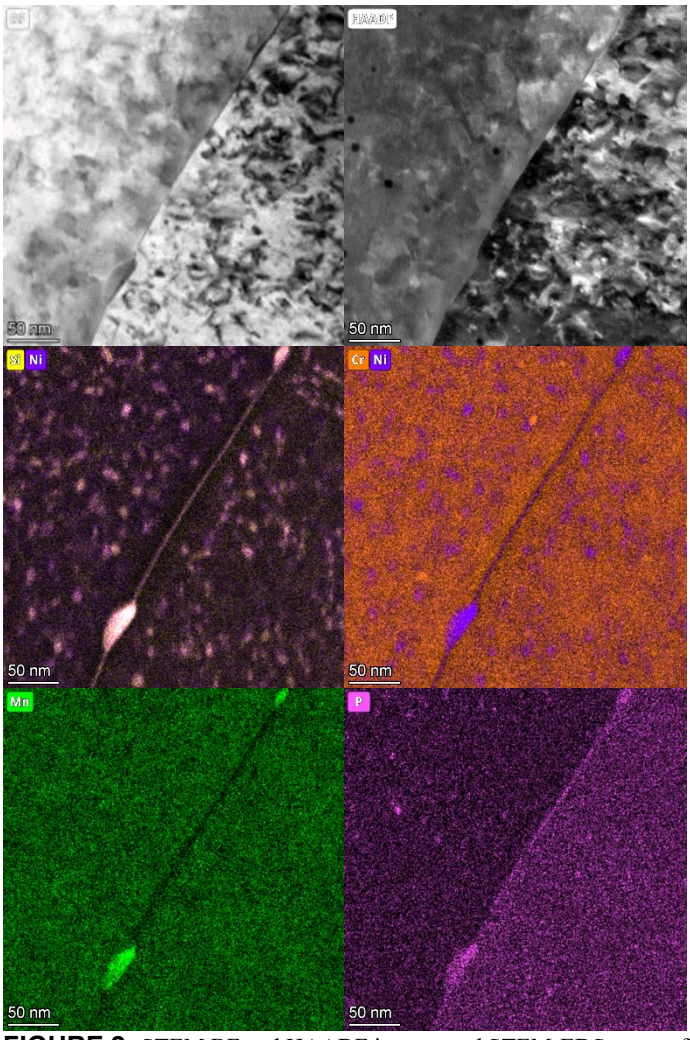

FIGURE 2: STEM BF and HAADF images and STEM-EDS maps of a high angle grain boundary in the MS section of BFB-4412 showing Ni-Si, Cr, and P precipitation in the matrix, and Ni, Si, and P segregation and Ni-Si-Mn precipitation at the grain boundary

Cavity formation was also present in both BFBs but had large differences in distribution among the sections within each bolt. Fig. 3 shows under-focus TEM images near grain boundaries in the CS, MS, and BS sections of the BFB 4412. The BS and MS sections have a distribution of large cavities (~8 nm in diameter) and small cavities (~2 nm in diameter), while the CS section has a high density of only small cavities (~2 nm in diameter). Similar cavity distributions were present in the low dose BFB 4416 [4]. The larger cavities are indicative of gradients along the bolt length in temperature, strain, fast/thermal neutron energy, and potentially hydrogen concentration from transmutation [1]. The thermal and strain gradients provide the excess energy for more vacancy emission from dislocation loops as they grow in the bolt thread (BS) and mid-shank (MS) sections than the bolt head section (CS). In addition, the vacancy and transmutant H/He mobility follows these thermal and strain gradients towards the bolt shank/ threads where they can gather into vacancy clusters and grow into large cavities that could be

gas-filled. This is consistent with what was seen in the BFB #4416 [4], with analysis of a baffle-former bolt retrieved from the Tihange 1 reactor [8], and with variation in void swelling in thick components [20]. Interestingly, within ~30 nm of the grain boundary in the MS section and within ~50 nm of the grain boundary in the BS section, there appears to be a denuded zone with much fewer large cavities. This denuded zone, as indicated by the yellow arrows, shows the influence of the grain boundary as a sink for defects, consistent with neutron irradiated 316 stainless steels studied elsewhere [21]. The grain boundary in the MS section Fig. 3 is the same one from Fig. 2. Interestingly, the size of the precipitate denuded zone and the large cavity denuded zone are about the same, which means these are interconnected with Ni and Si moving towards the grain boundary and vacancies moving away from the grain boundary. More work is needed to confirm if the grain boundary character influences the cavity grain boundary denuded zone.

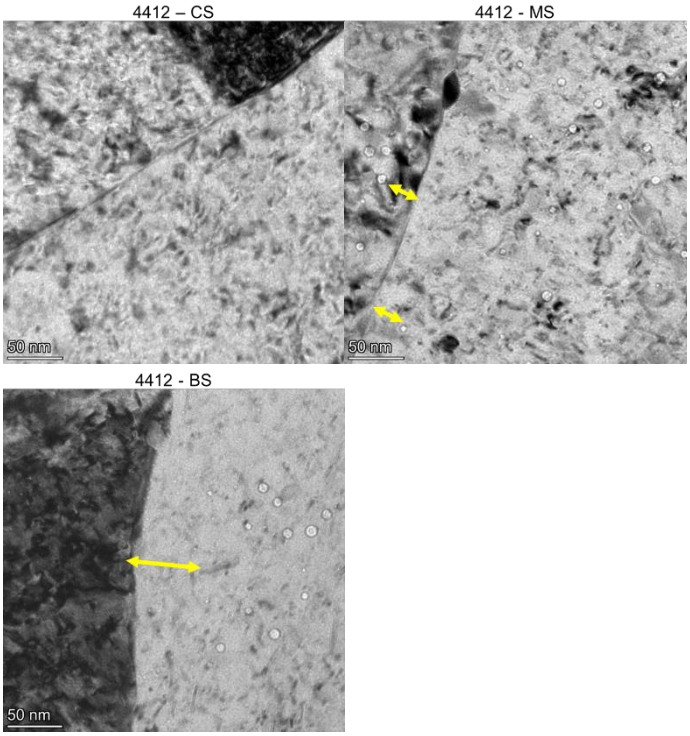

FIGURE 3: Under-focus TEM bright field images showing nano-scale cavities near grain boundaries in the CS, MS, and BS sections of BFB #4412

APT characterization was used to complement the TEM/STEM characterization, as it is a technique that enables higher spatial and compositional resolution all in three spatial dimensions. Here, APT data was collected from the matrix of each section of both BFBs. Reconstructions have been completed for four sharpened tips from each of the three sections in the BFB 4412 and one tip from each section in BFB 4416 – future work will target the grain boundaries. Fig. 4 depicts the Si, Ni, Mo, and Cu atom reconstructions, and Fig. 5 depicts the Si-6at%, Ni-20at%, Mo-5at%, and Cu-3at% isosurface reconstructions from one tip from each section of the BFB 4412. Qualitatively in Fig. 4, there is clear clustering of Ni and Si together, while there is also Cu clustering in all three reconstructions that does not directly overlap with the Ni and Si reconstructions. There also appears to be some Mo clustering, but it is quite faint relative to the background. The isosurface reconstructions in Fig. 5 more clearly show the trends for formation of Ni-Si-rich particles, Cu-rich clusters, and Mo-rich clusters. There appears to be a larger fraction of Ni-Si precipitation in the BS and MS reconstructions than in the CS, as shown by the green and grey isosurfaces. However, the number density of small Ni-Si precipitates appears larger in the CS; a point confirmed through quantitative analysis in Fig. 6 and Fig. 7. The red Mo and orange Cu isosurfaces do not overlap with the Ni-Si isosurfaces but in many cases appear attached to the Ni-Si isosurfaces. Though to be clear, not all Ni/Si isosurfaces have Mo or Cu isosurfaces attached to them. To more fully understand the dynamics, quantification of cluster size and number density is necessary.

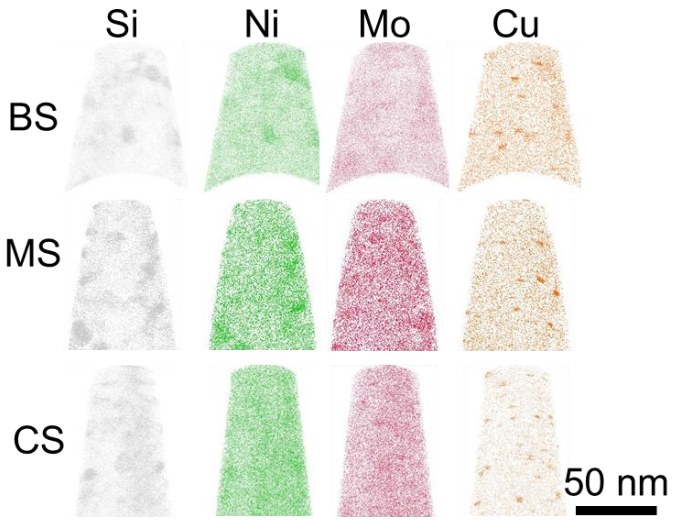

FIGURE 4: Atom reconstructions of Si, Ni, Mo, and Cu atoms from a select reconstruction of each section of the BFB #4412 – BS, MS, and CS. The reconstructions here are 30 nm in thickness

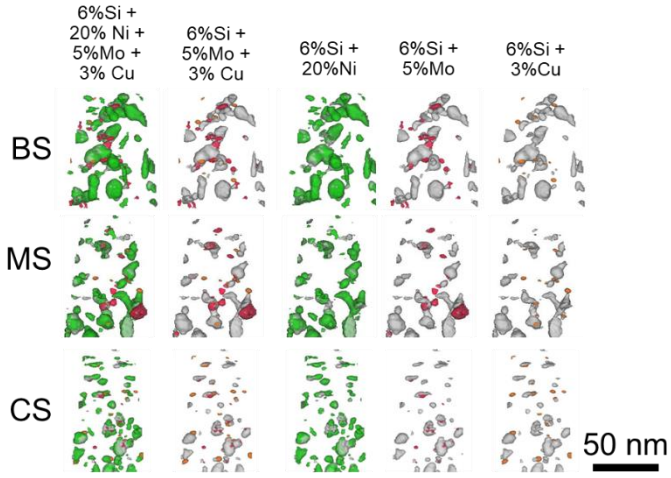

FIGURE 5: Isosurface reconstructions of same regions as in Fig. 4, though through the full thickness of the reconstruction. Green isosurfaces are of 20at% Ni, gray isosurfaces are of 6at% Si, red isosurfaces are of 5at% Mo, and orange isosurfaces are of 3at% Cu.

APT characterization allows for a high degree of quantification beyond standard visualization. Figs. 6, 7, and 8 shows the volume fraction, average spherical-equivalent radius, and number density of Ni-20at%, Si-6at%, and Cu-3at% isosurfaces averaged over the four reconstructions from each section of the BFB 4412 and the one reconstruction from each section. The volume fraction of Ni and Si isosurfaces is highest in the BS section and lowest in the CS section, while the opposite is true for the number density. This is the case for both BFBs. The average radius follows a similar trend as volume fraction for the Ni and Si isosurfaces, but the BS and MS sections have similar sizes. On the other hand, the volume fraction and number density of Cu isosurfaces is highest in the CS section compared to the BS and MS sections, while the sizes of the Cu isosurfaces are approximately the same in all sections. Not shown here, but the Mo isosurfaces have no trends in volume fraction, radius, or number density [6]. There are two primary points of interest from these results: Ni-Si precipitation is a thermally-activated diffusion-based process, while Cu-rich precipitation appears to be an athermal radiation-induced nucleation process.

Prior research has shown that the bolt thread (BS) and shank (MS) sections are hotter than the bolt head (CS) section [9]. In a diffusion-based process, particles will grow with increased time at the same temperature and will grow with increasing temperature. This is exactly what is seen in the Ni and Si isosurface data in Figs. 6 and 7. First, the number density of Ni and Si isosurfaces is approximately the same or higher in the low dose BFB 4416 compared to the high dose BFB 4412, meaning that radiation helps nucleate these particles even at a relatively low temperature. With respect to growth with increasing temperature, the BS and MS sections have larger volume fractions than the CS section in both bolts. Thus, it can be concluded that the BS and MS sections are hotter than the CS section. The difference in the volume fraction between the BS and CS sections relative to each bolt is the proof of the diffusion process. The volume fraction and size in the low temperature regime in the CS section does not increase much from BFB 4416 to BFB 4412. However, the volume fraction and size of Ni-Si isosurfaces increase dramatically in the high temperature regimes in the BS and MS sections from BFB 4416 to BFB 4412. This is consistent with precipitation and growth of Ni-Si-rich G-phase clusters relative to time and temperature during aging in the ferrite phase of duplex stainless steels [16]. Interestingly, previous research has shown that dislocation loop formation and RIS largely reach a saturation level at a dose of ~5 dpa [2]; it is clear from this work that Ni-Si precipitation is not saturated at least to doses of that the low dose BFB 4416 (15-29 dpa).

The case for Cu clustering being an athermal process lies in the fact that the size, volume fraction, and number density effectively are the same between the two BFBs relative to each section and that Cu clustering is highest in the lowest temperature section, CS. Cu is likely to phase separate at any elevated temperature due to its low miscibility in Fe and Cr. Thus, Cu precipitation has a higher dependency on vacancy concentration than on vacancy or atomic mobility, whereas Ni/Si precipitation may have the opposite dependency. Thus, radiation-induced vacancy concentration enables nucleation of Cu clusters. This makes sense as the miscibility of Cu in many metals is quite low, and therefore, the activation energy to phase separate for Cu is also low [22]. On the other hand, the solubility of Ni and Si in FCC Fe is higher; therefore, more energy in the form of thermal energy is needed to cause phase separation. Ballistic mixing during radiation generally favors dissolution of Ni and Si into FCC Fe, while the thermal spikes during irradiation are enough to cause Cu precipitation, independent of temperature, but as the temperature rises, ballistic mixing of Ni and Si is overcome by back diffusion due to a bias for phase separation [23]. As would be expected if this were true, the volume fraction and number density would be similar or slightly lower for the Cu clusters in the low dose bolt, while the Ni/Si-rich clusters will likely have a smaller radius but similar number density. The initial data from one reconstruction in each section in BFB 4416 demonstrates this analysis to be correct. This would be consistent with Cu-rich precipitation and Mn-Ni-Si-rich precipitation in reactor pressure vessel steels [24,25].

The effects of precipitation on mechanical behavior may largely be found in the hardness data [4] and to a lesser extent the fracture toughness [5]. As shown in those DOE reports, the hardness is greatly increased in all sections of both bolts and the fracture toughness is greatly reduced. There is also a small trend in hardness follows that of volume fraction of Ni-Si precipitates. The difference in hardness among the sections is small within BFB 4416 just as the difference in Ni-Si volume fraction is small in BFB 4416. However, the hardness is increases further as the precipitate volume fraction increases in BFB 4412. While the differences in hardness are small, the trend could be meaningful. The same trend in the drop of fracture toughness is observed as well, though only the BS and MS sections were tested.

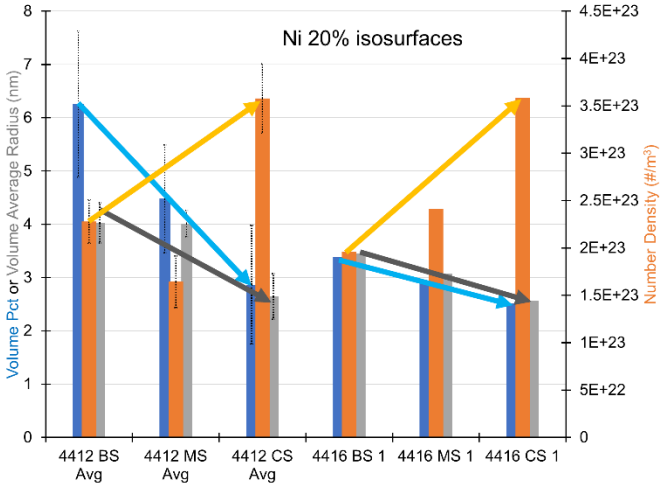

FIGURE 6: Volume percent (in blue), volumetric average spherical equivalent radius (in gray), and number density (in orange) of 20 at% Ni isosurfaces averaged over four reconstructions for each section of the BFB 4412 but only one reconstruction for BFB 4416. Error bars represent one standard deviation for BFB 4412.

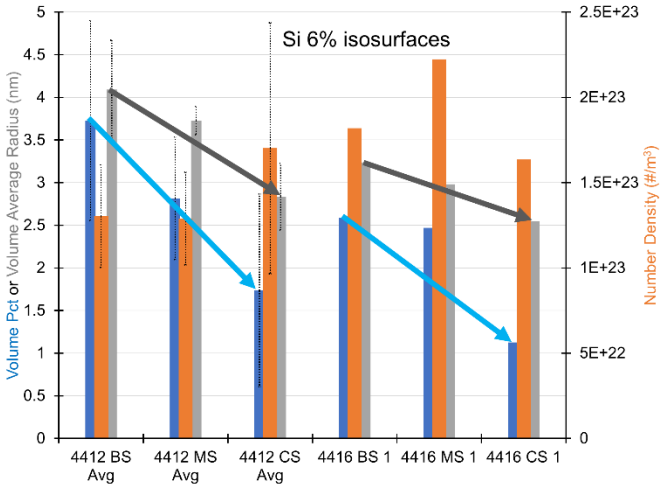

FIGURE 7: Volume percent (in blue), volumetric average spherical equivalent radius (in gray), and number density (in orange) of 6 at% Si isosurfaces averaged over four reconstructions for each section of the BFB 4412 but only one reconstruction for BFB 4416. Error bars represent one standard deviation for BFB 4412.

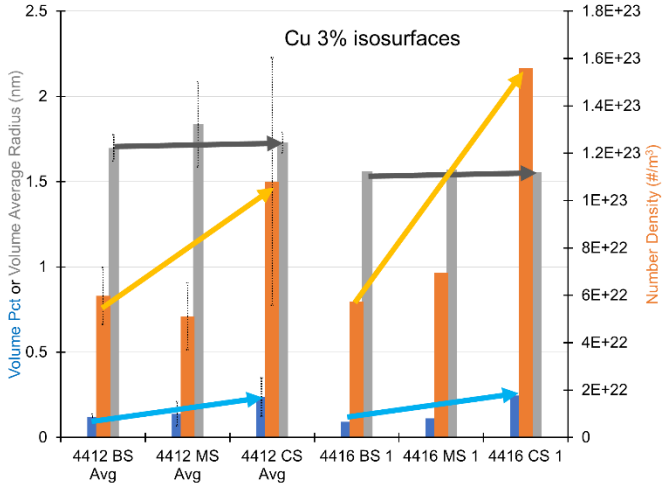

FIGURE 8: Volume percent (in blue), volumetric average spherical equivalent radius (in gray), and number density (in orange) of 3 at% Cu isosurfaces averaged over four reconstructions for each section of the BFB 4412 but only one reconstruction for BFB 4416. Error bars represent one standard deviation for BFB 4412.

As depicted in Fig. 5, clusters of different compositions form adjacent to each other. Ni-Si isosurfaces form the largest clusters while Mo and Cu surfaces are present on opposite sides of the main Ni-Si surfaces. Digging deeper into this aspect of 'co-clustering', Fig. 9 shows the 2D concentration contour plots and 1D concentration profile in the plane of a Cu/Si/Mo isosurface from a reconstruction of a tip in section BS of the BFB 4412. There is a center Ni-Si-rich precipitate with a diameter of ~10 nm that has a composition similar to Ni_3Si with a Cu-rich precipitate on the left side and a Cr/Mo/P-rich precipitate on the right side. Mn does not segregate into the precipitates but remains in the matrix; as such, the matrix precipitates are not G-phase that is similarly found in aged or irradiated ferritic steels or occasionally found at the grain boundary in the BS and MS sections (see Fig. 2). The Cr-Mo-P-rich phase could be an α` domain, but this is unverified. Interestingly, co-precipitates of Cu/Ni-Si-Mn/Mo were identified in thermally aged ferrite in duplex stainless steels [16], and co-precipitates of Cu-Ni-Si/Mo-Cr were found in the matrix of a 304 austenitic stainless steel retrieved from a commercial BWR power plant [26]. However, no tri-precipitates of Cu/Ni-Si/Mo-Cr-(P) without Mn in the Ni-Si phase have been observed to our knowledge in thermally aged or irradiated 304/316 type austenitic stainless steels. From this and previous research, the surfaces of either the Cu-rich or Ni-Si-rich phases serve as good nucleation sites for precipitation of either or both phases. Analysis of even lower dose materials would be necessary to determine which phase serves as the primary nucleation site, but it is likely that Cu would serve as such since it was found to be the case in thermal aging of duplex stainless steels [27]. The effect of this 'co-clustering' on mechanical behavior is still unknown.

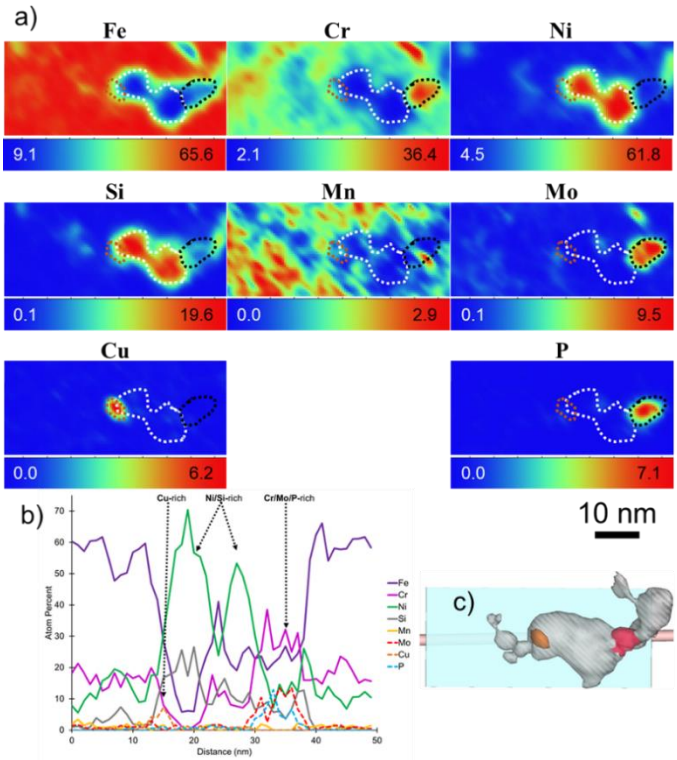

FIGURE 9: a) 2D concentration contour plots and b) 1D concentration profile through a co-precipitate of a Cu-rich precipitate adjacent to a Ni/Si-rich precipitate adjacent to a Cr/Mo/P-rich precipitate from BS section of BFB 4412 (same reconstruction in Fig. 4/5). White dots encircle the Ni-Si-rich cluster, black dots encircle the Cr/Mo/P-rich cluster, and orange dots encircle the Cu-rich cluster. c) Cu, Si, and Mo isosurfaces with box and cylinder from which a) and b) are taken from.

4. CONCLUSION

Complex radiation-induced microstructural evolution in austenitic stainless steel baffle former bolts retrieved from a commercial PWR was observed via TEM, STEM and APT. Three primary changes were observed: 1. radiation-induced grain boundary segregation of Ni, Si, and P, 2. precipitation of multiphase particles, and 3. formation and growth of cavities. These changes, particularly the precipitation and cavity formation, depended strongly irradiation temperature and less on irradiation dose. The gradient in these microstructural evolution features may help understand the failure mechanisms in these nuclear reactor internal components.

ACKNOWLEDGEMENTS

This research was sponsored by the U.S. Department of Energy, Office of Nuclear Energy, Light Water Reactor Sustainability Program, Materials Research Pathway, under contract DE-AC05-00OR22725 with UT-Battelle, LLC/Oak Ridge National Laboratory (ORNL). Atom probe tomography (APT) research was conducted as part of a user project at the Center for Nanophase Materials Sciences (CNMS), which is a US Department of Energy, Office of Science User Facility at Oak Ridge National Laboratory. We would like to thank Jonathan Poplawsky and James Burns for help with APT data collection. The authors extend their appreciation to Clay Morris, Jerid Metcalf, Mark Delph, and other colleagues at Irradiated Materials Examination and Testing Facility (IMET) at ORNL for their support during sample processing in the hot cell sample retrieval. In addition, we would like to thank Patricia Tedder and Travis Dixon at the Low Activation Materials Development and Analysis (LAMDA) Laboratory at ORNL, where mechanical behavior and TEM/STEM evaluation was conducted. We acknowledge Heather Malikowski and Robert Marcello of Exelon Corporation and Bernard Rudell formerly of Exelon Corporation for their assistance during the bolt harvesting process. Lastly, we would like to thank the late Mike Burke formerly with Electrical Power Research Institute who was involved in the bolt harvesting and characterization planning and led the sample preparation, machining, and shipping when he was working at Westinghouse Electric Company.

REFERENCES

[1] F.A. Garner, 3.02 - Radiation-Induced Damage in Austenitic Structural Steels Used in Nuclear Reactors☆, in: R.J.M. Konings, R.E.B.T.-C.N.M. (Second E. Stoller (Eds.), Elsevier, Oxford, 2020: pp. 57–168. https://doi.org/https://doi.org/10.1016/B978-0-12-803581-8.12067-3.

[2] O.K. Chopra, A.S. Rao, Degradation of LWR Core Internal Materials due to Neutron Irradiation, 2010.

[3] Stress Corrosion Cracking in Light Water Reactors: Good Practices and Lessons Learned, INTERNATIONAL ATOMIC ENERGY AGENCY, Vienna, 2011. https://www.iaea.org/publications/8671/stress-corrosion-cracking-in-light-water-reactors-good-practices-and-lessons-learned.

[4] X. (Frank) Chen, T. Chen, C.M. Parish, T. Graening, M.A. Sokolov, K.J. Leonard, Post-Irradiation Examination of High Fluence Baffle-Former Bolts Retrieved from a Westinghouse Two-Loop Downflow Type PWR, ORNL/TM-2019/1251, United States, 2019. https://doi.org/10.2172/1557483.

[5] X. (Frank) Chen, M.A. Sokolov, Fracture Toughness and Fatigue Crack Growth Rate Testing of Baffle-Former Bolts Harvested from a Westinghouse Two-Loop Downflow Type PWR, ORNL/TM-2021/2264, 2021.

[6] T.G. Lach, X. (Frank) Chen, T.M. Rosseel, Microstructural characterization of the second high fluence baffle-former bolt retrieved from a Westinghouse two-loop downflow type PWR, 2022.

[7] H.T. Tang, Materials Reliability Program Determination of Operating Parameters of Extracted Bolts (MRP-52), report number 1003076, EPRI technical report, 2001.

[8] D.J. Edwards, E.P. Simonen, F.A. Garner, L.R. Greenwood, B.M. Oliver, S.M. Bruemmer, Influence of irradiation temperature and dose gradients on the microstructural evolution in neutron-irradiated 316SS, J. Nucl. Mater. 317 (2003) 32–45.

https://doi.org/10.1016/S0022-3115(03)00003-5.
[9] M.R. Ickes, J. McKinley, J.-K. Lee, J.M. Smith, A.M. Ruminski, M.A. Burke, Irradiation-assisted stress corrosion cracking of Type 347 and Type 316 steels irradiated in commercial pressurized water reactors, J. Nucl. Mater. 536 (2020) 152182. https://doi.org/10.1016/j.jnucmat.2020.152182.
[10] C.M. Parish, K.G. Field, A.G. Certain, J.P. Wharry, Application of STEM characterization for investigating radiation effects in BCC Fe-based alloys, J. Mater. Res. 30 (2015) 1275–1289. https://doi.org/10.1557/jmr.2015.32.
[11] C.M. Parish, Chapter 5 - Multivariate Statistics Applications in Scanning Transmission Electron Microscopy X-Ray Spectrum Imaging, in: P.W.B.T.-A. in I. and E.P. Hawkes (Ed.), Adv. Imaging Electron Phys., Elsevier, 2011: pp. 249–295. https://doi.org/10.1016/B978-0-12-385983-9.00005-3.
[12] A. Devaraj, D.E. Perea, J. Liu, L.M. Gordon, T.J. Prosa, P. Parikh, D.R. Diercks, S. Meher, R.P. Kolli, Y.S. Meng, S. Thevuthasan, Three-dimensional nanoscale characterisation of materials by atom probe tomography, Int. Mater. Rev. 63 (2018) 68–101. https://doi.org/10.1080/09506608.2016.1270728.
[13] A. Devaraj, T.C. Kaspar, S. Ramanan, S. Walvekar, M.E. Bowden, V. Shutthanandan, R.J. Kurtz, Nanoscale phase separation in epitaxial Cr-Mo and Cr-V alloy thin films studied using atom probe tomography: Comparison of experiments and simulation, J. Appl. Phys. 116 (2014) 193512. https://doi.org/10.1063/1.4901465.
[14] J. Zhou, J. Odqvist, M. Thuvander, P. Hedström, Quantitative Evaluation of Spinodal Decomposition in Fe-Cr by Atom Probe Tomography and Radial Distribution Function Analysis, Microsc. Microanal. 19 (2013) 665–675. https://doi.org/10.1017/S1431927613000470.
[15] O.C. Hellman, J.A. Vandenbroucke, J. Rüsing, D. Isheim, D.N. Seidman, Analysis of Three-dimensional Atom-probe Data by the Proximity Histogram, Microsc. Microanal. 6 (2000) 437–444. https://doi.org/10.1007/S100050010051.
[16] T.G. Lach, D.A. Collins, T.S. Byun, Evolution of the role of molybdenum in duplex stainless steels during thermal aging: From enhancing spinodal decomposition to forming heterogeneous precipitates, J. Nucl. Mater. 557 (2021) 153268. https://doi.org/10.1016/j.jnucmat.2021.153268.
[17] R. Hu, G.D.W. Smith, E.A. Marquis, Effect of grain boundary orientation on radiation-induced segregation in a Fe–15.2at.% Cr alloy, Acta Mater. 61 (2013) 3490–3498. https://doi.org/10.1016/j.actamat.2013.02.043.
[18] T.G. Lach, A. Devaraj, K.J. Leonard, T.S. Byun, Co-dependent microstructural evolution pathways in metastable δ-ferrite in cast austenitic stainless steels during thermal aging, J. Nucl. Mater. 510 (2018) 382–395. https://doi.org/10.1016/j.jnucmat.2018.08.038.
[19] W.-Y. Chen, M. Li, M.A. Kirk, P.M. Baldo, T. Lian, Effect of heavy ion irradiation on microstructural evolution in CF8 cast austenitic stainless steel, J. Nucl. Mater. 471 (2016) 184–192. https://doi.org/10.1016/j.jnucmat.2015.08.032.
[20] Y. Huang, J.M.K. Wiezorek, F.A. Garner, P.D. Freyer, T. Okita, M. Sagisaka, Y. Isobe, T.R. Allen, Microstructural characterization and density change of 304 stainless steel reflector blocks after long-term irradiation in EBR-II, J. Nucl. Mater. 465 (2015) 516–530. https://doi.org/10.1016/j.jnucmat.2015.06.031.
[21] C.M. Barr, P.J. Felfer, J.I. Cole, M.L. Taheri, Observation of oscillatory radiation induced segregation profiles at grain boundaries in neutron irradiated 316 stainless steel using atom probe tomography, J. Nucl. Mater. 504 (2018) 181–190. https://doi.org/10.1016/j.jnucmat.2018.01.053.
[22] S.W. Chee, B. Stumphy, N.Q. Vo, R.S. Averback, P. Bellon, Dynamic self-organization in Cu alloys under ion irradiation, Acta Mater. 58 (2010) 4088–4099. https://doi.org/10.1016/j.actamat.2010.03.039.
[23] R.A. Enrique, P. Bellon, Compositional Patterning in Systems Driven by Competing Dynamics Of Different Length Scale, Phys. Rev. Lett. 84 (2000) 2885–2888. https://doi.org/10.1103/PhysRevLett.84.2885.
[24] N. Almirall, P.B. Wells, S. Pal, P.D. Edmondson, T. Yamamoto, K. Murakami, G.R. Odette, The mechanistic implications of the high temperature, long time thermal stability of nanoscale Mn-Ni-Si precipitates in irradiated reactor pressure vessel steels, Scr. Mater. 181 (2020) 134–139. https://doi.org/10.1016/j.scriptamat.2020.02.027.
[25] M. Mamivand, P. Wells, H. Ke, S. Shu, G.R. Odette, D. Morgan, CuMnNiSi precipitate evolution in irradiated reactor pressure vessel steels: Integrated Cluster Dynamics and experiments, Acta Mater. 180 (2019) 199–217. https://doi.org/10.1016/j.actamat.2019.09.016.
[26] T.G. Lach, M.J. Olszta, S.D. Taylor, K.H. Yano, D.J. Edwards, T.S. Byun, P.H. Chou, D.K. Schreiber, Correlative STEM-APT characterization of radiation-induced segregation and precipitation of in-service BWR 304 stainless steel, J. Nucl. Mater. 549 (2021) 152894. https://doi.org/10.1016/j.jnucmat.2021.152894.
[27] T.G. Lach, W.E. Frazier, J. Wang, A. Devaraj, T.S. Byun, Precipitation-site competition in duplex stainless steels: Cu clusters vs spinodal decomposition interfaces as nucleation sites during thermal aging, Acta Mater. 196 (2020) 456–469. https://doi.org/10.1016/j.actamat.2020.05.017.